Modeling epithelial and endothelial cell tropism for SARS-CoV-2 through restricted transgenic hACE2 expression in mice

Author list

Sahine Lameire[1,2]*, Nincy Debeuf[1,2]*, Julie Deckers[1,2], Caroline De Wolf[1,2], Manon Vanheerswynghels[1,2], Wendy Toussaint[1,2], Lize De Vlieger[3,4], Lien Van Hoecke[3,4], Sieglinde De Cae[5,6], Bert Schepens[5,6], Stijn Vanhee[1,2,7] and Bart N. Lambrecht[1,2,8]

*These authors contributed equally to this work

Affiliations

1. Laboratory of Immunoregulation and Mucosal Immunology, VIB Center for Inflammation Research, Ghent, Belgium.
2. Department of Internal Medicine and Pediatrics, Ghent University, Ghent, Belgium.
3. Barriers in Inflammation, VIB Center for Inflammation Research, Ghent, Belgium.
4. Department of Biomedical Molecular Biology, Ghent University, Ghent, Belgium.
5. VIB Center for Medical Biotechnology, Ghent, Belgium.
6. Department of Biochemistry and Microbiology, Ghent University, Ghent, Belgium.
7. Department of Head and Skin, Ghent University, Ghent, Belgium.
8. Department of Pulmonary Medicine, Erasmus University Medical Center Rotterdam, Rotterdam, Netherlands.

Corresponding author: Bart.lambrecht@ugent.be

Abstract

Given the ongoing evolution of SARS-CoV-2 and the historical emergence of other highly transmissible coronaviruses like SARS-CoV and HCoV-NL63, *in vivo* coronavirus research remains crucial even when the COVID-19 pandemic is receding. Due to restricted tropism of SARS-CoV-2 and other coronaviruses for mouse cells, model systems of infection rely on transgenic expression of the entry receptor human ACE2 (hACE2). Available hACE2 transgenic models using the *Krt18* promotor express the receptor across multiple cell types and organ systems, leading to multiple disease features including pneumonia, vascular compromise and neuro-inflammation, that reflect the multi-organ nature of COVID-19. To disentangle the role of cell tropism in driving the clinical manifestations of the disease, we generated two new transgenic mouse models, *Sftpa1*-hACE2 and *Cdh5*-hACE2 transgenic mice, with hACE2 restricted to lung epithelium or endothelial cells respectively. In *Sftpa1*-hACE2 mice, with high expression of the hACE2 receptor in lung alveolar type 2 cells, SARS-CoV-2 infection led to rapidly progressing disease, characterised by a strong neutrophilic innate immune response in the lung, followed by viral neuro-invasion and early death. *Krt18*-hACE2 mice additionally recruited various dendritic cell subsets and gradually developed adaptive immunity. In *Cdh5*-hACE2 Tg mice with exclusive endothelial tropism of the virus, viral inoculation via the lung or systemic circulation did not lead to viral propagation or disease manifestations, despite endothelial expression of hACE2 in the lung. These results suggest that tropism for alveolar epithelial cells increases disease severity, while endothelial cell tropism *per se* does not drive the vascular consequences often seen in COVID-19 patients. Our new transgenic mouse models will be helpful to dissect how cell tropism contributes to the clinical manifestations of coronavirus infection.

Introduction

Severe acute respiratory syndrome coronavirus 2 (SARS-CoV-2) is the causative agent of COVID-19, which escalated into a global pandemic in 2020. SARS-CoV-2 is an enveloped, positive-sense, single-stranded RNA virus belonging to the genus *Betacoronaviridae* (Lu et al., 2020). Two other highly transmissible and pathogenic coronaviruses (CoVs), Severe Acute Respiratory Syndrome coronavirus (SARS-CoV) and Middle East Respiratory Syndrome coronavirus (MERS-CoV), have emerged in humans, raising worldwide concerns (Wit et al., 2016). Other coronaviridae, such as the alphacoronavirus HCoV-NL63, can cause more milder upper respiratory disease (Abdul-Rasool and Fielding, 2010). The severity of COVID-19 cases varies from asymptomatic to those experiencing severe acute respiratory distress syndrome with possible fatal outcomes (Li et al., 2021). Whereas SARS-CoV-2 initially replicates in the upper airways, the typical clinical manifestations of severe COVID-19 are mostly related to the lower respiratory system, such as pneumonia, cough, shortness of breath, and acute respiratory distress syndrome (ARDS) (Hu et al., 2021) . However, despite being a respiratory tract infection, COVID-19 got quickly labelled as a multi-organ-disease as a broad range of other symptoms were reported, such as diarrhea (intestinal pathology), proteinuria (kidney disease), strokes and seizures caused by thromboembolic events or encephalitis, and cardiac and vascular inflammation (Hu et al., 2021). This wide array of clinical manifestations seen in COVID-19 patients could be explained by the broad distribution of ACE2 receptors across various organs, but does not necessarily reflect direct cell or tissue tropism of the virus (Oudit et al., 2023). ACE2 is the receptor used by the highly pathogenic SARS-CoV-2, SARS-CoV but also by the milder HCoV-NL63 structural Spike (S) protein to enter the host cells (Hofmann et al., 2005; Lan et al., 2020; Li et al., 2003). In normal physiology, ACE2 plays an integral role in the renin-angiotensin system, regulating vasoconstriction, blood pressure and coagulation. In pathophysiology, ACE2 contributes to fibrosis, tissue remodeling and endothelial dysfunction (Baldari et al., 2023; Oudit et al., 2023). In addition to allowing direct infection, interference with ACE2 might therefore also contribute to disease features.

Various mouse model systems have been created to model SARS-CoV-2 infection *in vivo* and track the development and resolution of COVID-19 disease (Asaka et al., 2021; Bao et al., 2020; Dinnon et al., 2020; Dong et al., 2021; Golden et al., 2020; Hassan et al., 2020; Jiang et al., 2020; Leist et al., 2020; Liu et al., 2024; Oladunni et al., 2020; Snouwaert et al., 2023; Song et al., 2024; Sun et al., 2020; Winkler et al., 2020). Due to structural differences in mouse and human ACE2 proteins, the real-world pathogenic SARS coronaviruses exhibit poor tropism for

mouse tissues, and infection is inefficient in mice (Ni et al., 2023) . To overcome this limitation, *in vivo* model systems depend on the heterologous expression of human ACE2 (hACE2) in mice. The most widely used transgenic mouse model for COVID-19 is the *Krt18*-hACE2 model, in which the expression of hACE2 is driven by the cytokeratin 18 (*Krt18*) promoter resulting in epithelial cell-specific expression of hACE2, primarily in the airways and lung and to a lesser extent in other tissues like kidney, liver, spleen and small intestine (Dong et al., 2021; Golden et al., 2020; Oladunni et al., 2020; Winkler et al., 2020). Although infection of *Krt18*-hACE2 mice cannot fully replicate the clinical spectrum of COVID-19, it provides a valuable platform for studying the interplay of multiple processes involved in disease progression. Disease outcome is a sum of different contributions resulting from direct infection across various cell types and organ systems, as well as their cascading indirect effects on other organ systems, including cardiovacular thromboembolic events (Bonaventura et al., 2021; Kandhaya-Pillai et al., 2022; Xu et al., 2023; Zhang et al., 2024). To model the effects of initial cell tropism in tissues that matter for disease severity, we therefore generated two new transgenic mouse models with hACE2 expression restricted to either epithelial cells of the lower lung or to endothelial cells. In *Sftpa1*-hACE2 mice, the *Surfactant Protein A1* promoter was chosen to drive hACE2 expression specifically in alveolar type II cells that are located in the alveoli of the lung, where pneumonia and ARDS develop. In order to model COVID-19 related vascular symptoms, such as coagulopathy and thromboembolic events, we also generated *Cdh5*-hACE2 mice, which express hACE2 under control of the *Cadherin 5* gene promotor, to restrict expression to endothelial cells. Using these new models in comparison with the wide-spread Krt18-hACE2 model, we performed an in-depth pathological analysis after SARS-CoV-2 infection including clinical illness, viral replication, viral tropism, and histopathology of several organs.

Results

SARS-CoV-2 severity depends on restricted hACE2 expression

In an attempt to disentangle some of the clinical features seen in COVID-19 patients, we generated two new transgenic mouse models characterised by different hACE2 expression patterns, either driven by the *Sftpa1* promotor or the *Cdh5* promotor, and compared these with widely available *Krt18*-hACE2 mice (Fig.1A) (Dong et al., 2021; Golden et al., 2020; Oladunni et al., 2020; Winkler et al., 2020). A detailed description of the generation of the transgenic lines is provided in the Materials and Methods section. Both quantitative PCR (RT-qPCR) and Western blotting showed clear and significant expression of hACE2 in the lungs of all transgenic mice in comparison to non-transgenic wild type littermates (WT) (Fig.1B,C).

We first performed titration experiments to find the optimal inoculum dose of the European D614G strain (EVAg) in *Krt18*-hACE2 mice, a fully established mouse model for COVID-19 (Dong et al., 2021; Golden et al., 2020; Oladunni et al., 2020; Winkler et al., 2020). Intratracheal (i.t.) infection with 450 plaque forming units (pfu) resulted in *Krt18*-hACE2 mice displaying an average reduction of 8,06% ± 1.65 in their body weight at 7 dpi accompanied by respiratory distress and reduced mobility. By 11 dpi, when the survivor mice had regained their initial weight, only 50% of *Krt18*-hACE2 mice had survived (Fig.2A). Non-transgenic wild type littermates were infected with an identical viral dose as control, but were not susceptible to infection. *Sftpa1*-hACE2 mice exhibited a more severe disease progression compared to the *Krt18*-hACE2 mice when administered an identical viral dose (450 pfu). At 4 dpi, *Sftpa1*-hACE2 animals lost more than 15% of their initial body weight, paralleled by the manifestation of additional symptoms of pathogenic SARS-CoV-2 infection, including reduced mobility, signs of respiratory distress and neurological symptoms (shaking, twitching, hypersalivation and seizures) (Fig.2A, Fig.4A). Consequently, mice had to be sacrificed due to their high disease score, reaching the humane endpoint. By contrast, *Cdh5*-hACE2 mice, with hACE2 expression restricted to endothelial cells, did not lose weight nor displayed clinical signs of disease when infected via inhalation of the same dose (450 pfu) of viral inoculum. To circumvent the fact that lung tissue damage might be necessary for the virus to reach the hACE2 viral entry receptor on the endothelium, we bypassed this barrier by also infecting a separate group of *Cdh5*-hACE2 mice intravenously with a very high viral dose (10^4 pfu). However, intravenous infection still did not cause illness in these mice (Fig.2B).

To unravel the underlying mechanism of disease severity, mice of the various lines were sacrificed one day prior to reaching the anticipated humane endpoint. Expression of the virion-associated N gene was present in lungs of both *Sftpa-hACE2* and *Krt18-hACE2* lines (Fig.2C). As these data can also involve input challenge virus, we also quantified S-gene expression, which indicates active viral gene expression (Fig.2D). Again, S-gene was highly detected in all transgenic lines except for the *Cdh5*-hACE2 line, but was most pronounced in the *Krt18*-hACE2 line. To distinguish and quantify infectious viral particles (viral titer), a plaque assay on VeroE6/TMPRSS2 cells was performed (Fig.2E). Samples were weighed post-collection for normalisation. In *Krt18*-hACE2 mice, the viral titer in the lung was strongly elevated at 4 dpi and was drastically reduced by 7 dpi. Infectious viral particles were slightly increased in *Sftpa1*-hACE2 mice compared to WT mice at 4 dpi, but could no longer be ascertained in *Sftpa1*-hACE2 mice since they reached humane endpoint. On histological examination of the lungs one day prior to reaching the anticipated humane endpoint, we observed perivascular and peribronchial immune cell infiltration exclusively in the lungs of the *Krt18*-hACE2 Tg mice, but not in the other transgenic lines (Fig.2F). Overall, *Sftpa1*-hACE2 Tg mice show a more rapid disease progression with death despite a lower viral titer and despite less pathological damage in the lung than the *Krt18*-hACE2 mice. The latter exhibit both clinical signs of infection and subsequent recovery, making this model more suited for studying the full course of disease progression and resolution. Despite clear expression of hACE2 in lung endothelium, Cdh5-hACE2 mice were not susceptible to infection, nor did they develop vascular problems.

<u>Immune cell influx in the lung upon SARS-CoV-2 infection is dependent on the hACE2 expression pattern</u>

As both *Sftpa1*- and *Krt18*-hACE2 mice had elevated viral titers in the lung, but different disease parameters, and discordant histopathology, we wondered whether pulmonary inflammation would be discretely altered. Therefore, we performed multicolour flow cytometry on lung tissue and quantified the number of infiltrating immune cells, while adhering to the stringent biosafety measures imposed in a Biosafety Level 3 lab. *Sftpa1*-hACE2 Tg mice had a significant increase in the number of $CD11b^{+}Ly6G^{+}$ neutrophils in the lung, whereas the number of other innate immune cells was not altered (Fig.3A-C). An increase in neutrophils was also observed in *Krt18*-hACE2 Tg females, but only at 7 dpi, consistent with the delayed disease progression in *Krt18*-hACE2 mice compared to *Sftpa1*-hACE2 mice. At 7 dpi, *Krt18*-hACE2 mice also displayed a massive influx of $CD88^{+}CD11b^{+}Ly6C^{+}$-monocytes in the lung, whereas $SiglecF^{+}CD11c^{hi}$ AMs were reduced (Fig.3B-C). This AM "disappearance" reaction

after viral infection has been described before (Barman et al., 2022; Debeuf et al., 2024; Singh et al., 2024). At 4 dpi, CD8 T cells, and not CD4 T cells, were significantly elevated in *Krt18*-hACE2 mice compared to wildtype mice, and this increase was even more pronounced at 7 dpi (Fig.3D-E). This was accompanied by robust IFN-γ production in the lung, suggesting activation of the infiltrating T cells (Fig.3F). Immune cell numbers were not altered in lungs of *Cdh5*-hACE2 mice compared to wildtype mice (Fig.3A-F).

Next, we zoomed in on dendritic cells (DCs), as these are the cells responsible for CD8 and CD4 T cell priming. A gating strategy was employed to distinguish monocyte-derived cells (MCs) ($CD88^+$) from conventional DCs ($CD26^+$)(Fig. 3G). We have recently shown that upon viral infection, inflammatory cDC2s (FcεRI+ cDC2s) arise, with capacities shared with both cDC1s (XCR1+) and cDC2s (CD172a+) (Bosteels et al., 2020). Upon SARS-CoV-2 infection, all DC subtypes were strongly present in the lungs *of Krt18*-hACE2 mice (Fig.3H-K). Interestingly, inf-cDC2s were already the most pronounced DC subtype at 4 dpi. Infl-cDC2s have been shown to be dependent on type I interferon signalling (Bosteels et al. 2020), and indeed both at 4 and 7 dpi, interferon-response genes such as *Isg15*, *Oas*, and *Cxcl9* were elevated in the lung of *Krt18*-hACE2 Tg mice. Overall, an early and strong neutrophilic innate immune response was detected in *Sftpa1*-hACE2 mice. However, mice succumbed to the infection before any functional adaptive response could be engaged. Our findings reveal profound changes in the lungs of SARS-CoV-2-infected *Krt18*-hACE2 mice, characterized by delayed neutrophil cell influx, loss of resident macrophages, and increased interferon responses steering inflammatory cDC2s, compared with *Sftpa1*-hACE2 mice.

<u>Robust viral replication in the brain of *Sftpa1* mice, accompanied by neurological symptoms</u>

As previously mentioned, i.t. SARS-CoV-2 infection (450 pfu) resulted in severe weight loss in *Sftpa1*-hACE2 animals at 4 dpi. This was paralleled by additional symptoms of pathogenic SARS-CoV-2 infection, including reduced mobility and signs of respiratory distress. Interestingly, several mice also endured neurological symptoms like shaking, twitching, hypersalivation and seizures (Fig. 4A). A number of *Sftpa1*-hACE2 mice also developed severe symptoms in the intestine which appeared macroscopically bloated and orange in colour, suggestive of impaired enteric or autonomic nervous system function affecting intestinal homeostasis. This phenotype has previously been reported (Stolp et al., 2022). H&E staining on the small intestine confirmed these abnormalities. Severe villous atrophy could be observed

in the small intestine, characterized by a marked reduction in villous height and blunting of the normal finger-like projections (Suppl. Figure 1). In addition, the intestinal wall exhibited thinning of the mucosal and submucosal layers, with a loss of structural integrity.

Given the severe neurological symptoms observed in the *Sftpa1*-hACE2 Tg mice, we conducted a deeper examination of the brain. Western blotting revealed hACE2 protein in the brain of all three hACE2 transgenic lines, which was unexpected in the *Sftpa1*-hACE2 line. However, although surfactant protein A is typically expressed by alveolar epithelial type 2 cells, contributing to the reduction of alveolar surface tension in the lungs, its presence has also been demonstrated in the brain (Scheffzük et al., 2024). To distinguish and quantify infectious viral particles in the brain (viral titer), a plaque assay on VeroE6/TMPRSS2 cells was performed (Fig. 4C). Samples were weighed post-collection for normalisation. Interestingly, *Sftpa1*-hACE2 mice had a high viral titer in the brain, potentially linked to the occurrence of the neurological symptoms in these mice. In female *Krt18*-hACE2 mice, by 7 dpi, SARS-CoV-2 tropism also shifted towards the brain, whereas no viral load was detected in male mice at that timepoint. To confirm neuro-invasion by SARS-CoV-2, we performed confocal imaging on brain sections with an anti-nucleocapsid antibody against the virion. In both *Sftpa1*-hACE2 at 4 dpi and female *Krt18*-hACE2 mice at 7 dpi, we could detect SARS-CoV-2 virus dispersed in the brain. Remarkably, in none of the readouts, SARS-CoV-2 could be detected in *Cdh5*-hACE2 mice, suggesting that hACE2 expression on endothelial cells solely did not favour infection by the virus. Conclusively, SARS-CoV-2 infection results in robust viral replication in the lungs of *Krt18*-hACE2 mice, which is accompanied by delayed neutrotropism, whereas *Sftpa1*-hACE2 mice had a high viral titer in the brain with lower replication in the lung.

Discussion

Because clinically relevant strains of SARS-CoV-2 hardly infect mice, model systems for COVID-19 have to rely on the heterologous expression of hACE2. In addition to the commonly used *Krt18*-hACE2 transgenic mice, several other mouse lines have been generated and tested such as HFH4-hACE2, CMV-hACE2 and *mAce2*-hACE2 mice (Asaka et al., 2021; Jiang et al., 2020; Liu et al., 2024; Snouwaert et al., 2023; Song et al., 2024). Variations in hACE2 expression across tissues and cell type tropism have been shown to result in differential viral replication in various organs, influencing disease outcome and presentation. Most model designs prioritize achieving sufficient hACE2 expression in the respiratory tract to support SARS-CoV-2 infection, although this might not reflect physiological hACE2 expression patterns (Baldari et al., 2023; Oudit et al., 2023). An alternative approach to facilitate the use of mice as a model system for SARS-CoV-2 research has been the adaptation of the human virus to infect mice. Several mouse-adapted virus strains have been developed by serial passage of the virus in the lungs of mice (Dinnon et al., 2020; Leist et al., 2020). This approach offers a key advantage as it enables the immediate application of numerous mouse knockout lines and disease models in the study of this coronavirus. This strategy also has inherent limitations, as the effectiveness is restricted by its dependence on the murine rather than human ACE2 expression pattern for binding to host cells. Notable differences in lung expression patterns of ACE2 have been observed: while the murine promoter primarily drives expression in airway club cells, the human promoter targets alveolar type 2 (AT2) cells (Snouwaert et al., 2023) .

Here, we constructed *Sftpa1*-hACE2 mice, in which the hACE2 is directed towards AT2 cells. The mice showed clinical manifestations such as severe weight loss, respiratory distress and neurological symptoms. To our surprise, these mice also expressed hACE2 in the brain, and not only in the lung as would be expected by using the *Sftpa1*-promoter. As a result, these mice had high viral titers in the brain and probably died from brain damage. In contrast, in human COVID-19 patients, evidence for neurotropism and neuroinvasion is sparce (Khan et al., 2022; Lebrun et al., 2023). Although expression of *Sftpa1* in the brain has been described previously (Pocha et al., 2020; Scheffzük et al., 2024)aberrant tissue expression of the *Sftpa1*-carrying Bacterial Artificial Chromosome (BAC) construct that was used to create our *Sftpa1*-hACE2 mice could also be an explanation for brain expression. Transgene insertion in the *Sftpa1* locus on the BAC disrupts intronic enhancers, or interferes with cis-regulatory interactions of the promotor, potentially explaining leakiness of expression to the brain. Nevertheless, this model might be useful to model brain-specific COVID-19 related pathologies. The widely used *Krt18*-

hACE2 mice also showed evidence for brain infection, yet later in the disease course, in line with earlier reports (Oladunni et al., 2020; Winkler et al., 2020). The strongest advantage of the *Krt18*-hACE2 model is the fact that they show a dose-response relationship and a recovery post infection. This model has therefore been used for testing the efficacy of therapies and treatments like neutralizing antibodies (Cae et al., 2023). The transgenic hACE2 lines were established through the random integration of a transgene into the mouse genome, typically resulting in a multicopy array. A notable limitation in our study is the absence of precise information regarding the genomic localization and copy number of the hACE2 insertions. Such information would have been valuable for elucidating the heightened susceptibility of *Sftpa1*-hACE2 mice to SARS-CoV-2 infection.

From the very start of the COVID-19 pandemic, it has been clear that many patients suffer from thromboembolic events, and since endothelial cells express ACE2, it was logical to assume that this was caused by direct infection by the virus. While we did not assess this in our study, electron microscopy observations in COVID-19 patients have revealed that SARS-CoV-2 can indeed directly infect endothelial cells (ECs) (Varga et al., 2020). Also the alphacoronavirus HCoV-NL63 can infect endothelial cell lines *in vitro*, by binding to hACE2 (Hofmann et al., 2005) . Elevated levels of circulating ECs and soluble markers of endothelial derangement have been detected in severe COVID-19, indicating EC apoptosis and breakdown of the endothelial barrier (Falcinelli et al., 2021). Beyond direct infection by SARS-CoV-2, ECs can also be damaged by systemic inflammation driven by a cytokine storm. Pro-inflammatory cytokines like IL-6, IL-1β, TNF-α and MCP-1, as well as complement activation pathways, also aggravate multi-organ injury by perpetuating the vicious cycle of ECs damage, endothelial inflammation and thrombosis (Bonaventura et al., 2021; Damme et al., 2023; Declercq et al., 2021). This was the motivation to also create *Cdh5*-hACE2 mice, with virus tropism restricted to endothelial cells. We validated that these mice had hACE2 in their lungs, but clinical signs of infection, viral replication and histopathological changes post SARS-CoV-2 infection were absent. To circumvent the fact that lung tissue damage might be necessary for the virus to reach the endothelially located hACE2 receptor, we also infected *Cdh5*-hACE2 mice intravenously. However, intravenous infection did not alter the outcome in these mice. Systemic inflammation may be necessary in order to create an inflammatory environment where full endothelial dysfunction can be established. Alternatively, endothelial cells might not express the proteases that are needed to unwind the S protein after binding to hACE2. Future studies in these mice could investigate how systemic inflammation facilitates endothelial infection by creating a

permissive environment for SARS-CoV-2, potentially uncovering key mechanisms underlying endothelial damage, thrombosis, and multi-organ failure in severe COVID-19 cases.

One striking observation was that *Sftpa1*-hACE2 mice had accelerated innate immune neutrophilic responses. Previous work in influenza A virus infection has shown that intense neutrophilic inflammation of the lung can contribute to clinical severity and mortality (Brandes et al., 2013), but we have not directly studied if neutrophil depletion would increase survival in the *Sftpa*-hACE2 mice. On the other hand, the accumulation of inflammatory cDC2s, cells that share features of cDC1 and cDC2, and therefore present viral antigens to both cDC1 and cDC2 (Bosteels et al., 2020) occurred were delayed kinetics in *Sftpa1*-hACE2 mice compared with *Krt18*-hACE2 mice. Accelerated appearance of inf-cDC2 was associated with better induction of adaptive immunity in *Krt18*-hACE2 strain, although we did not deplete DCs to prove the causality of this association, like we did in earlier work on viral infection of the lungs (Bosteels et al., 2020; GeurtsvanKessel et al., 2009). We noticed a sexual dimorphism upon SARS-CoV-2 infection, especially in *Krt18*-hACE2 Tg mice. For instance, male *Krt18*-hACE2 mice had a stronger IFN response compared to their female counterparts, and an increased number of inf-cDC2s, which are IFN dependent (Bosteels et al., 2020). On the other hand, female *Krt18*-hACE2 exhibited more neutrophilia in the lungs and SARS-CoV-2 tropism shifted towards the brain at 7 dpi, which was not the case in male mice.

In conclusion, by restricting hACE2 expression to lung type 2 alveolar epithelial cells, we created mice with increased susceptibility to severe COVID-19, including neurological manifestations. By finding little infectivity in mice with endothelial tropism for the SARS-CoV2 virus, we question the idea that primary infection of endothelial cells is a major contributor to disease, although this could clearly be different when multiple cell types are infected and signs of systemic inflammation develop.

Figure Legends

Fig 1: A. Schematic overview of the hACE2-transgenic mice with their corresponding primary expected tissue expression of the hACE2 receptor and graphical representation of the constructs used to generate the hACE2 transgenic lines. **B.** RT-qPCR analysis of *hAce2* mRNA expression in lung tissue of steady-state hACE2 transgenic mice. **C.** Western blot analysis of hACE2 protein in the lung of steady state hACE2-transgenic mice and accompanying β-tubulin loading controls. Samples were normalized to the same protein concentrations before loading on gel. WT = wildtype, F = female, M = male.

Data are shown as means ± SEM. Male mice are displayed in filled dots while females are represented with open dots. After assessing normality by a Shapiro-Wilk normality test, non-parametric data were analysed with a Kruskal-Wallis test, where each transgenic line was compared to WT. $**p < 0.01$; $****p < 0.0001$.

Fig 2: A. Weight loss and survival curve of hACE2-transgenic mice (6-12 weeks old) after intratracheal SARS-CoV-2 infection (450 pfu). Data represent 6-20 mice per group, pooled from three separate experiments, and are shown as means ± SEM. **B.** Weight loss of *Cdh5*-hACE2 mice (6-12 weeks old) after intravenous SARS-CoV-2 infection (10^4 pfu). Data represents 6 mice per group and are shown as means ± SEM. **C/D:** RT-qPCR results of N- and S-gene expression in post-caval lung lobe of SARS-CoV-2 infected hACE2 transgenic mice (i.t., 450 pfu) 4 and 7 days post infection. The virion associated N gene represents total viral RNA present in the sample (relative to an internal standard), regardless of whether the virus is infectious or not, while the S-gene represents viral gene expression relative to house-keeping-genes. Male mice are displayed in filled dots while females are represented with open dots. **E:** Determination of infectious viral progeny by plaque assay on VeroE6/TMPRSS2 cells of homogenised lung samples of SARS-CoV-2 infected hACE2 transgenic mice (i.t., 450 pfu) 4 and 7 days post infection (PFU/mg). PFU, plaque-forming units. Male mice are displayed in filled dots while females are represented with open dots. **F**. Representative H&E-stained lung sections from hACE2 Tg mice on 4 dpi (*Sftpa1*) or 7 dpi (*Krt18* and *Cdh5*). Scale bar = 200 μm.

Statistics: After assessing normality by a Shapiro-Wilk normality test, parametric data were analysed with a One-way ANOVA or an unpaired *t*-test (B); and non-parametric data were analysed with a Kruskal-Wallis test. The statistics of the survival data was tested with the

Kaplan-Meier test. Each transgenic line was compared to WT. $*p \leq 0.05$; $**p < 0.01$; $***p < 0.001$; $****p < 0.0001$.

Fig 3:

A-E, H-K. Flow cytometric measurements of inflammatory cells in the lung of SARS-CoV-2 infected mice (i.t., 450 pfu) 4 and 7 days post infection. Data are shown as means ± SEM. Male mice are displayed in filled dots while females are represented with open dots.

G. Gating strategy to distinguish DC subsets presented in H-K

F, L-N. Relative mRNA expression of *Ifn-γ*, *Isg15*, *Oas* and *Cxcl9* in the post-caval lung lobe of SARS-CoV-2 infected hACE2 Tg mice (i.t., 450 pfu) 4 and 7 days post infection.

Statistics: After assessing normality by a Shapiro-Wilk normality test, parametric data were analysed with a One-way ANOVA; and non-parametric data were analysed with a Kruskal-Wallis test. Each transgenic line was compared to WT. $*p \leq 0.05$; $**p < 0.01$; $***p < 0.001$; $****p < 0.0001$.

Fig 4

A: Schematic overview of the clinical signs observed post intratracheal SARS-CoV-2 infection with 450 pfu. Each row represents a hACE2-transgenic line and columns represent the number of days post infection. Weight-loss and lethargic symptoms are gradual measurements, where a darker shade represents worse symptoms, while respiratory distress, neurological symptoms and gas-filled intestine are discontinuous measurements meaning if the mice experienced the signs, the pie is filled. The pie represents both males and females.

B: Western blot analysis of hACE2 protein in the brain of steady state hACE2-transgenic mice and accompanying β-tubulin loading controls. Samples were normalized to the same protein concentrations before loading on gel.

C: Determination of infectious viral progeny by Plaque Assay on VeroE6/TMPRSS2 cells of homogenised brain samples of SARS-CoV-2 infected hACE2 Tg mice (i.t., 450 pfu) 4 and 7 days post infection (PFU/mg). PFU, plaque-forming units. Male mice are displayed in filled dots while females are represented with open dots.

D: SARS-CoV-2 Nucleocapsid (N)-immunostaining (pink) in the brain of SARS-CoV-2 infected hACE2 Tg mice. In *Sftpa1*-hACE2 mice: 4 dpi, in *Krt18*- and *Cdh5*-hACE2 mice: 7 dpi. Scale bar = 200 μm.

Statistics: After assessing normality by a Shapiro-Wilk normality test, non-parametric data were analysed with a Kruskal-Wallis test. Each transgenic line was compared to WT. $*p \leq 0.05$; $****p < 0.0001$.

Supplementary Figure 1

Representative H&E-stained gut sections from hACE2 Tg mice on 4 dpi (*Sftpa1*) or 7 dpi (*Krt18* and *Cdh5*). Scale bar = 200 μm.

Material and Methods

Mice

Mice were housed under specific pathogen-free conditions and used between 6 and 12 weeks of age. All experiments were approved by the animal ethics committee at Ghent University (EC2023-097) and were in accordance with Belgian animal protection law. *Krt18*-hACE2 transgenic mice were purchased from The Jackson Laboratory (strain ID 034860). *Sftpa1*-hACE2 and *Cdh5*-hACE2 transgenic mice were generated in-house. Graphical representation of the constructs used to generate the lines can be found in Fig.1. For the *Sftpa1*-hACE2 line, a 2 kb region containing the mouse *Sftpa1* promoter and sequence upstream the *Sftpa1* start codon (exon 1 to 3 in transcript 202) was amplified from the mouse (bl6) genome using a proofreading polymerase and cloned into the expression vector pCAGGs using the XhoI restriction site. The hACE2 cDNA was excised from the pCAG-hACE2 vector and cloned into the *Sftpa1* start codon resulting in a transgenic construct in which hACE2 is expressed under the mouse *Sftpa1* promoter. A 5,4 kb SalI-NcoI fragment was isolated over gel, purified and injected into fertilized oocytes. For the *Cdh5*-hACE2 line, the BAC clone RP23-277P19 containing the mouse *Cdh5* locus was ordered at BACPAC Resources Center. The FRT-kan/neo-FRT selection cassette was cloned downstream the pA sequence of pCAG-hACE2 using HindIII (partial digestion) and the resulting construct was used as a template for amplification of the recombination fragment. hACE2-pA-FNF was inserted into the start codon of *Cdh5* in exon 2 of the BAC via Red/ET recombination. The selection cassette was subsequently removed by expression of Flpe in bacteria. The modified BAC was digested with PacI and a 32 kB transgenic fragment was separated over PFGE, purified from gel and injected into fertilized oocytes. All founders were genotyped using primers specific to hACE2.

SARS-CoV-2 infection

Mice were intratracheally infected with a sublethal dose of SARS-CoV-2 virus (450 pfu, SARS-CoV-2 D614G strain SARS-CoV-2/human/FRA/702/2020, obtained from the European Virus Archive (EVAG)). This virus was propagated on VeroE6/TMPRSS2 cells (NIBIOHN, JCRB1819) in Dulbecco's Modified Eagle Medium (DMEM) supplemented with 2% fetal bovine serum (FBS). Two days after infection the growth medium was collected. After centrifugation for 10 minutes at 1000 x g, the supernatant was collected, aliquoted and stored at –80°C. Virus titration was performed by plaque assay in which monolayers of VeroE6/TMPRSS2 cells were infected with dilutions series prepared in Dulbecco's Modified

Eagle Medium (DMEM) supplemented with 2% fetal bovine serum (FBS) in duplicate for 2 vials. Two hours after infection, Avicel was added to a final concentration of 0.3% (w/v). After 2 days of incubation at 37°C, the overlays were removed, and the cells were fixed with 3.7% paraformaldehyde (PFA) and stained with 0.5% crystal violet and counted. These experiments were performed in Biosafety Level 3 conditions at the VIB-UGent Center for Medical Biotechnology. All intratracheal treatments were given after mice were anesthetized with isoflurane (2 liters/min, 2 to 3%; Abbott Laboratories).

Tissue sampling

Mice were euthanized by cervical dislocation or an overdose of pentobarbital (KELA Laboratoria) and organs were collected.

Flow cytometry

Lung lobes were isolated, cut with scissors and then digested for 30 min in RPMI-1640 (Gibco, Thermo Fisher Scientific) containing 20 μg/ml liberase TM (Roche), 10 U/ml DNase I (Roche), and 5% of FCS (Bodinco) at 37°C. Next, lungs were filtered through a 70 μm cell strainer. Single cell suspensions were incubated with a mix of fluorescently labelled monoclonal antibodies (Ab) in the dark for 30 minutes at 4°C. To reduce non-specific binding, 2.4G2 Fc receptor Ab (Bioceros) was added. Dead cells were removed from analysis, using fixable viability dye eFluor506 or eFluor780 (Thermo Fisher Scientific). 123count eBeads Counting Beads (Thermo Fisher Scientific) were added to each sample to determine absolute cell numbers. Before acquisition, photomultiplier tube voltages were adjusted to minimize fluorescence spillover. Single-stain controls were prepared with UltraComp eBeads (Thermo Fisher Scientific) following the manufacturer's instructions and were used to calculate a compensation matrix. Sample acquisition was performed on a NovoCyte Quanteon flow cytometer (Agilent) equipped with NovoExpress software. Graphical output was performed using FlowJo software (Tree Star, Inc.) and GraphPad Prism 10 (GraphPad Software, Inc.).

The following antibodies were used: anti-CD26 (FITC, BioLegend), anti-CD172a (PerCP-eFluor710, eBioscience), anti-CD317 (BV421, BD Biosciences), anti-CD11c (BV605, BioLegend), anti-CD88 (BV711, BD Biosciences), anti-CD19 (BV786, BD Biosciences), anti-CD40 (APC, BD Biosciences), anti-CD45 (AF700, BioLegend), anti-MHCII (APC-Cy7, eBioscience), anti-XCR1 (PE, BioLegend), anti-FcεRI (biotin, Life Technologies), streptavidin-PE-CF594 (BD Biosciences), anti-CD3 (PE-Cy5, BioLegend), anti-NK1.1 (PE-Cy5, BioLegend), anti-Ter119 (PE-Cy5, BioLegend), anti-CCR7 (PE-Cy7, BioLegend), anti-

MHCII (FITC, eBioscience), anti-CD88 (PerCP-Cy5.5 BioLegend), anti-Ly6C (eFluor450, eBioscience), anti-CD11b (BV605, BioLegend), anti-Ly6G (BV650, BD Biosciences), anti-CD64 (BV711, BioLegend), anti-SiglecF (BV786, BD Biosciences), anti-CD45 (AF700, BioLegend), anti-bTCR (APC-eFluor780, BioLegend), anti-NK1.1 (PE, BD Biosciences), anti-CD11c (PE-TR, eBioscience), anti-CD4 (PE-Cy5, BioLegend), anti-CD8a (PE-Cy7, BioLegend).

Histology and confocal microscopy

During dissection, mice were transcardially perfused with PBS containing 0.002% heparin sodium followed by 1% PFA. After overnight fixation in 4% paraformaldehyde solution, lung and intestine were embedded in paraffin, cut into 5-µm slices, and stained with H&E. Images were taken with an AxioScan Slidescanner (Zeiss). For brain tissue, cryosections of 20 µm were cut and processed for immunostaining. For immunostainings, brain sections went through an extra round of fixation with 4% PFA, followed by blocking with 2% goat serum in PBS-T (PBS with 0.5% BSA and 0.3% Triton X-100) solution for 1 h at room temperature. The sections were then stained with primary antibodies (anti-Nucleocapsid-protein of SARS-CoV-2, SYSY, cat. HS-452 011) in blocking buffer at 4°C overnight. After washing with PBS, sections were stained with a AF633-conjugated goat-anti mouse secondary antibody (ThermoFisher Scientific) in blocking buffer for 2 h before washing and mounting. A Zeiss Axioscan Z.1 was used for imaging and images were processed using Zeiss Zen Software.

RNA isolation, cDNA synthesis, and quantitative PCR (qPCR)

Lung samples were collected and mechanically disrupted using Qiagen TissueLyser beads and bead mill. RNA was isolated using TRIzol LS Reagent (Thermo Fisher Scientific) according to the manufacturer's instructions. The cDNA was synthesized with the Sensifast cDNA synthesis kit (Bioline, Meridian Bioscience). qRT-PCR reactions were conducted in a LightCycler 480 (Roche) using the SensiFAST sybr no-ROX mix (Bioline). For the SARS-CoV-2 N-protein measurement Taqman PCR was performed using the LightCycler® TaqMan® Master (04535286001, Roche). Data were analyzed using qBASE software (BioGazelle).

Following primer pairs were used:

hACE2
Forward:GGGATCAGAGATCGGAAGAAGAAA,
Reverse:AGGAGGTCTGAACATCATCAGTG.

SC-2 N

Forward: TTACAAACATTGGCCGCAAA

Reverse: GCGCGACATTCCGAAGAA

Probe: FAM-ACAATTTGCCCCCAGCGCTTCAG-BHQ1

SC-2 S

Forward: CCTTCCCAGGTAACAAACCAACC

Reverse: ACACACTGACTAGAGACTAGTGGC

Ifn-γ

Forward: ATGAACGCTACACACTGCATC

Reverse: CCATCCTTTTGCCAGTTCCTC

Isg15

Forward: GGTGTCCGTGACTAACTCCAT

Reverse: TGGAAAGGGTAAGACCGTCCT

Oas1a

Forward: GCCTGATCCCAGAATCTATGC

Reverse: GAGCAACTCTAGGGCGTACTG

Cxcl9

Forward: GTGGAGTTCGAGGAACCCTAG

Reverse: ATTGGGGCTTGGGGCAAAC

Hprt

Forward: TCCTCCTCAGACCGCTTT

Reverse: CCTGGTTCATCATCGCTAATC

Rpl13a

Forward: CCTGCTGCTCTCAAGGTTGTT

Reverse: TGGTTGTCACTGCCTGGTACTT

Analysis of hACE2 protein expression by Western Blot

Organs were collected and mechanically homogenised using Qiagen TissueLyser beads and bead mill in RIPA buffer supplemented with cOmplete™ ULTRA protease inhibitor and PhosSTOP™ phosphatase inhibitor. The samples were vortexed and placed on a turner for 30

min at 4°C. Samples were centrifuged at 13000g for 10 min and the supernatant was used for Nano-orange protein measurement. Lysates were standardised to equal protein concentration and diluted in 4× Laemmli buffer containing 50 mM Tris-HCl pH 6.8, 2% sodium dodecyl sulphate (SDS), and 10% glycerol. Lysates were boiled for 10 min at 95 °C, proteins were separated by SDS-PAGE (8% gel) and transferred to a PVDF membrane. Immunoblotting was performed by overnight incubation at 4 °C using the anti-hACE2 primary antibody (ab108209, clone EPR4436, 1:1000, abcam) followed by a 2 h incubation at RT using the following secondary antibodies: HRP-linked anti-rabbit IgG (P0450, 1:1000, DAKO). As loading control, the blot was stained with anti-beta-tubulin-HRP (ab21058, abcam, 1:5000) 1,5 h on room temperature.

Determination of viral titers by plaque assay

Lung and brain were directly collected in 2 mL CK14 and 7 mL CK28 Precellys ® tubes respectively. Tubes were weight before and after collection to determine the weight of the organ. Samples were homogenised in the Precellys® homogeniser for 2 x 10 sec at 5000 rpm, with a 15 sec break in between and spun down to remove debris. Monolayers of VeroE6/TMPRSS2 cells were infected with dilutions series of the samples prepared in FB medium:Opti-MEM™ in duplicate (FB medium: FluoroBrite DMEM medium (ThermoFisher Scientific cat# A1896702) supplemented with 5% FCS, 4 mM L-glutamine, NaPyruvate and P/S). One hours after infection, Avicel was added to the wells to a final concentration of 0.4% (w/v). After 2 days of incubation at 37°C, the overlays were removed, and the cells were fixed with 4% paraformaldehyde (PFA) and stained with 0.5% crystal violet.

Statistical analysis

Data information: Data are shown as means ± SEM. All data were analysed with a Shapiro-Wilk normality test to assess whether the data was normally distributed and whether a parametric or non-parametric test was applicable. For each Figure, the statistical tests are mentioned in the figure legends.

Acknowledgements

We thank the VIB flow core and VIB transgenic core facility for their expert advice and service in this project. We thank Leen Vanhoutte and Tino Hochepied for their help in the generation of hACE2 transgenic mice. We thank Koen Sedeyn for providing training and service in the BSL3 facility at the VIB-UGent Center for Medical Biotechnology. We thank Arnout Bruggeman and Prof. Roos Vandenbroucke for their analysis of histopathological brain sections. This publication was supported by the European Virus Archive GLOBAL (EVA-GLOBAL) project that has received funding from the European Union's Horizon 2020 research and innovation programme under grant agreement No 871029.

Funding

N.D. acknowledges support from an FWO Postdoctoral Fellowship - junior grant (1258921N).

B.S. acknowledges EOS joint programme of Fonds de la recherche scientifique—FNRS and Fonds wetenschapellijk onderzoek–Vlaanderen—FWO (G0H7518N EOS ID: 30981113 and G0H7322N EOS ID: 40007527).

S.D.C. is a predoctoral fellow supported by the Research Foundation-Flanders, Belgium (FWO-Vlaanderen).

S.V. was a postdoctoral fellow of the Research Foundation-Flanders, Belgium (FWO-Vlaanderen; grant No. 1244321N) while working on this project and acknowledges support from FWO Vlaanderen senior research project grant No. G0A7422N.

B.N.L. acknowledges support from FWO Methusalem grant (01M01521), FWO EOS research grant (3G0H1222), IBOF grant (01M01521), and the Flanders Institute of Biotechnology (VIB).

References

Abdul-Rasool S, Fielding BC. 2010. Understanding Human Coronavirus HCoV-NL63. *Open Virol J* **4**:76–84. doi:10.2174/1874357901004010076

Asaka MN, Utsumi D, Kamada H, Nagata S, Nakachi Y, Yamaguchi T, Kawaoka Y, Kuba K, Yasutomi Y. 2021. Highly susceptible SARS-CoV-2 model in CAG promoter-driven hACE2 transgenic mice. *Jci Insight* **6**:e152529. doi:10.1172/jci.insight.152529

Baldari CT, Onnis A, Andreano E, Giudice GD, Rappuoli R. 2023. Emerging roles of SARS-CoV-2 Spike-ACE2 in immune evasion and pathogenesis. *Trends Immunol*. doi:10.1016/j.it.2023.04.001

Bao L, Deng W, Huang B, Gao H, Liu J, Ren L, Wei Q, Yu P, Xu Y, Qi F, Qu Y, Li F, Lv Q, Wang W, Xue J, Gong S, Liu M, Wang G, Wang S, Song Z, Zhao Linna, Liu P, Zhao Li, Ye F, Wang H, Zhou W, Zhu N, Zhen W, Yu H, Zhang X, Guo L, Chen L, Wang C, Wang Y, Wang X, Xiao Y, Sun Q, Liu H, Zhu F, Ma C, Yan L, Yang M, Han J, Xu W, Tan W, Peng X, Jin Q, Wu G, Qin C. 2020. The pathogenicity of SARS-CoV-2 in hACE2 transgenic mice. *Nature* **583**:830–833. doi:10.1038/s41586-020-2312-y

Barman TK, Singh AK, Bonin JL, Nafiz TN, Salmon SL, Metzger DW. 2022. Lethal synergy between SARS-CoV-2 and Streptococcus pneumoniae in hACE2 mice and protective efficacy of vaccination. *Jci Insight* **7**. doi:10.1172/jci.insight.159422

Bonaventura A, Vecchié A, Dagna L, Martinod K, Dixon DL, Tassell BWV, Dentali F, Montecucco F, Massberg S, Levi M, Abbate A. 2021. Endothelial dysfunction and immunothrombosis as key pathogenic mechanisms in COVID-19. *Nat Rev Immunol* **21**:319–329. doi:10.1038/s41577-021-00536-9

Bosteels C, Neyt K, Vanheerswynghels M, Helden MJ van, Sichien D, Debeuf N, Prijck SD, Bosteels V, Vandamme N, Martens L, Saeys Y, Louagie E, Lesage M, Williams DL, Tang S-C, Mayer JU, Ronchese F, Scott CL, Hammad H, Guilliams M, Lambrecht BN. 2020. Inflammatory Type 2 cDCs Acquire Features of cDC1s and Macrophages to Orchestrate Immunity to Respiratory Virus Infection. *Immunity* **52**:1039-1056.e9. doi:10.1016/j.immuni.2020.04.005

Brandes M, Klauschen F, Kuchen S, Germain RN. 2013. A Systems Analysis Identifies a Feedforward Inflammatory Circuit Leading to Lethal Influenza Infection. *Cell* **154**:197–212. doi:10.1016/j.cell.2013.06.013

Cae SD, Molle IV, Schie L van, Shoemaker SR, Deckers J, Debeuf N, Lameire S, Nerinckx W, Roose K, Fijalkowska D, Devos S, Desmet A-S, Marchan JCZ, Venneman T, Sedeyn K, Ballegeer M, Vanheerswynghels M, Wolf CD, Demol H, Vanhaverbeke P, Ghassabeh GH, Lonigro C, Bockstal V, Rinaldi M, Abdelnabi R, Neyts J, Marqusee S, Lambrecht BN, Callewaert N, Remaut H, Saelens X, Schepens B. 2023. Ultrapotent SARS coronavirus-neutralizing single-domain antibodies that bind a conserved membrane proximal epitope of the spike. *bioRxiv* 2023.03.10.531533. doi:10.1101/2023.03.10.531533

Damme KFAV, Hoste L, Declercq J, Leeuw ED, Maes B, Martens L, Colman R, Browaeys R, Bosteels C, Verwaerde S, Vermeulen N, Lameire S, Debeuf N, Deckers J, Stordeur P, Depuydt P, Braeckel EV, Vandekerckhove L, Guilliams M, Schetters STT, Haerynck F, Tavernier SJ, Lambrecht BN. 2023. A complement atlas identifies interleukin-6–dependent alternative pathway dysregulation as a key druggable feature of COVID-19. *Sci Transl Med* **15**:eadi0252. doi:10.1126/scitranslmed.adi0252

Debeuf N, Deckers J, Lameire S, Bosteels C, Hammad H, Lambrecht BN. 2024. Inhaled GM-CSF administered during ongoing pneumovirus infection alters myeloid and CD8 T cell immunity without affecting disease outcome. *Front Immunol* **15**:1439789. doi:10.3389/fimmu.2024.1439789

Declercq J, Damme KFAV, Leeuw ED, Maes B, Bosteels C, Tavernier SJ, Buyser SD, Colman R, Hites M, Verschelden G, Fivez T, Moerman F, Demedts IK, Dauby N, Schryver ND, Govaerts E, Vandecasteele SJ, Laethem JV, Anguille S, Hilst J van der, Misset B, Slabbynck H, Wittebole X, Liénart F, Legrand C, Buyse M, Stevens D, Bauters F, Seys LJM, Aegerter H, Smole U, Bosteels V, Hoste L, Naesens L, Haerynck F, Vandekerckhove L, Depuydt P, Braeckel E van, Rottey S, Peene I, Straeten CVD, Hulstaert F, Lambrecht BN. 2021. Effect of anti-interleukin drugs in patients with COVID-19 and signs of cytokine release syndrome (COV-AID): a factorial, randomised, controlled trial. *Lancet Respir Med* **9**:1427–1438. doi:10.1016/s2213-2600(21)00377-5

Dinnon KH, Leist SR, Schäfer A, Edwards CE, Martinez DR, Montgomery SA, West A, Yount BL, Hou YJ, Adams LE, Gully KL, Brown AJ, Huang E, Bryant MD, Choong IC, Glenn JS, Gralinski LE, Sheahan TP, Baric RS. 2020. A mouse-adapted model of SARS-CoV-2 to test COVID-19 countermeasures. *Nature* **586**:560–566. doi:10.1038/s41586-020-2708-8

Dong W, Mead H, Tian L, Park J-G, Garcia JI, Jaramillo S, Barr T, Kollath DS, Coyne VK, Stone NE, Jones A, Zhang J, Li A, Wang L-S, Milanes-Yearsley M, Torrelles JB, Martinez-Sobrido L, Keim PS, Barker BM, Caligiuri MA, Yu J. 2021. The K18-hACE2 Transgenic Mouse Model Recapitulates Non-Severe and Severe COVID-19 in Response to Infectious Dose of SARS-CoV-2 Virus. *J Virol* JVI0096421. doi:10.1128/jvi.00964-21

Falcinelli E, Petito E, Becattini C, Robertis ED, Paliani U, Sebastiano M, Vaudo G, Guglielmini G, Paciullo F, Cerotto V, Malvestiti M, Gori F, Bury L, Lazzarini T, Gresele P, investigators C study. 2021. Role of endothelial dysfunction in the thrombotic complications of COVID-19 patients. *J Infect* **82**:186–230. doi:10.1016/j.jinf.2020.11.041

GeurtsvanKessel CH, Willart MAM, Bergen IM, Rijt LS van, Muskens F, Elewaut D, Osterhaus ADME, Hendriks R, Rimmelzwaan GF, Lambrecht BN. 2009. Dendritic cells are crucial for maintenance of tertiary lymphoid structures in the lung of influenza virus–infected mice. *J Exp Med* **206**:2339–2349. doi:10.1084/jem.20090410

Golden JW, Cline CR, Zeng X, Garrison AR, Carey BD, Mucker EM, White LE, Shamblin JD, Brocato RL, Liu J, Babka AM, Rauch HB, Smith JM, Hollidge BS, Fitzpatrick C, Badger CV, Hooper JW. 2020. Human angiotensin-converting enzyme 2 transgenic mice infected with SARS-CoV-2 develop severe and fatal respiratory disease. *Jci Insight* **5**:e142032. doi:10.1172/jci.insight.142032

Hassan AO, Case JB, Winkler ES, Thackray LB, Kafai NM, Bailey AL, McCune BT, Fox JM, Chen RE, Alsoussi WB, Turner JS, Schmitz AJ, Lei T, Shrihari S, Keeler SP, Fremont DH, Greco S, McCray PB, Perlman S, Holtzman MJ, Ellebedy AH, Diamond MS. 2020. A SARS-CoV-2 Infection Model in Mice Demonstrates Protection by Neutralizing Antibodies. *Cell* **182**:744-753.e4. doi:10.1016/j.cell.2020.06.011

Hofmann H, Pyrc K, Hoek L van der, Geier M, Berkhout B, Pöhlmann S. 2005. Human coronavirus NL63 employs the severe acute respiratory syndrome coronavirus receptor for cellular entry. *Proc Natl Acad Sci* **102**:7988–7993. doi:10.1073/pnas.0409465102

Hu B, Guo H, Zhou P, Shi Z-L. 2021. Characteristics of SARS-CoV-2 and COVID-19. *Nat Rev Microbiol* **19**:141–154. doi:10.1038/s41579-020-00459-7

Jiang R-D, Liu M-Q, Chen Y, Shan C, Zhou Y-W, Shen X-R, Li Q, Zhang L, Zhu Y, Si H-R, Wang Q, Min J, Wang X, Zhang W, Li B, Zhang H-J, Baric RS, Zhou P, Yang X-L, Shi Z-L. 2020. Pathogenesis of SARS-CoV-2 in Transgenic Mice Expressing Human Angiotensin-Converting Enzyme 2. *Cell* **182**:50-58.e8. doi:10.1016/j.cell.2020.05.027

Kandhaya-Pillai R, Yang X, Tchkonia T, Martin GM, Kirkland JL, Oshima J. 2022. TNF-α/IFN-γ synergy amplifies senescence-associated inflammation and SARS-CoV-2 receptor expression via hyper-activated JAK/STAT1. *Aging Cell* **21**:e13646. doi:10.1111/acel.13646

Khan M, Clijsters M, Choi S, Backaert W, Claerhout M, Couvreur F, Breda LV, Bourgeois F, Speleman K, Klein S, Laethem JV, Verstappen G, Dereli AS, Yoo S-J, Zhou H, Do TND, Jochmans D, Laenen L, Debaveye Y, Munter PD, Gunst J, Jorissen M, Lagrou K, Meersseman P, Neyts J, Thal DR, Topsakal V, Vandenbriele C, Wauters J, Mombaerts P, Gerven LV. 2022. Anatomical barriers against SARS-CoV-2 neuroinvasion at vulnerable interfaces visualized in deceased COVID-19 patients. *Neuron* **110**:3919-3935.e6. doi:10.1016/j.neuron.2022.11.007

Lan J, Ge J, Yu J, Shan S, Zhou H, Fan S, Zhang Q, Shi X, Wang Q, Zhang L, Wang X. 2020. Structure of the SARS-CoV-2 spike receptor-binding domain bound to the ACE2 receptor. *Nature* **581**:215–220. doi:10.1038/s41586-020-2180-5

Lebrun L, Absil L, Remmelink M, Mendonça RD, D'Haene N, Gaspard N, Rusu S, Racu M-L, Collin A, Allard J, Zindy E, Schiavo AA, Clercq SD, Witte OD, Decaestecker C, Lopes M-B, Salmon I. 2023. SARS-Cov-2 infection and neuropathological findings: a report of 18 cases and review of the literature. *Acta Neuropathol Commun* **11**:78. doi:10.1186/s40478-023-01566-1

Leist SR, Dinnon KH, Schäfer A, Tse LV, Okuda K, Hou YJ, West A, Edwards CE, Sanders W, Fritch EJ, Gully KL, Scobey T, Brown AJ, Sheahan TP, Moorman NJ, Boucher RC, Gralinski LE, Montgomery SA, Baric RS. 2020. A Mouse-Adapted SARS-CoV-2 Induces Acute Lung Injury and Mortality in Standard Laboratory Mice. *Cell* **183**:1070-1085.e12. doi:10.1016/j.cell.2020.09.050

Li J, Luo H, Deng G, Chang J, Qiu X, Liu C, Qin B. 2021. Multidimensional Evaluation of All-Cause Mortality Risk and Survival Analysis for Hospitalized Patients with COVID-19. *Int J Méd Sci* **18**:3140–3149. doi:10.7150/ijms.58889

Li W, Moore MJ, Vasilieva N, Sui J, Wong SK, Berne MA, Somasundaran M, Sullivan JL, Luzuriaga K, Greenough TC, Choe H, Farzan M. 2003. Angiotensin-converting enzyme 2 is a functional receptor for the SARS coronavirus. *Nature* **426**:450–454. doi:10.1038/nature02145

Liu G, Zhang M, Wu B, Zhang C, Wang Yan, Han X, Wang R, Li L, Wei Y, Sun Yali, Cao X, Wang Yuan, Li Y, Li M, Zhao G, Ke Y, Guo Z, Yin Q, Sun Yansong. 2024. A highly susceptible hACE2-transgenic mouse model for SARS-CoV-2 research. *Front Microbiol* **15**:1348405. doi:10.3389/fmicb.2024.1348405

Lu R, Zhao X, Li J, Niu P, Yang B, Wu H, Wang W, Song H, Huang B, Zhu N, Bi Y, Ma X, Zhan F, Wang L, Hu T, Zhou H, Hu Z, Zhou W, Zhao L, Chen J, Meng Y, Wang J, Lin Y, Yuan J, Xie Z, Ma J, Liu WJ, Wang D, Xu W, Holmes EC, Gao GF, Wu G, Chen W, Shi W, Tan W. 2020. Genomic characterisation and epidemiology of 2019 novel coronavirus: implications for virus origins and receptor binding. *Lancet* **395**:565–574. doi:10.1016/s0140-6736(20)30251-8

Ni D, Turelli P, Beckert B, Nazarov S, Uchikawa E, Myasnikov A, Pojer F, Trono D, Stahlberg H, Lau K. 2023. Cryo-EM structures and binding of mouse and human ACE2 to SARS-CoV-2 variants of concern indicate that mutations enabling immune escape could expand host range. *PLOS Pathog* **19**:e1011206. doi:10.1371/journal.ppat.1011206

Oladunni FS, Park J-G, Pino PA, Gonzalez O, Akhter A, Allué-Guardia A, Olmo-Fontánez A, Gautam S, Garcia-Vilanova A, Ye C, Chiem K, Headley C, Dwivedi V, Parodi LM, Alfson KJ, Staples HM, Schami A, Garcia JI, Whigham A, Platt RN, Gazi M, Martinez J, Chuba C, Earley S, Rodriguez OH, Mdaki SD, Kavelish KN, Escalona R, Hallam CRA, Christie C, Patterson JL, Anderson TJC, Carrion R, Dick EJ, Hall-Ursone S, Schlesinger LS, Alvarez X, Kaushal D, Giavedoni LD, Turner J, Martinez-Sobrido L, Torrelles JB. 2020. Lethality of SARS-CoV-2 infection in K18 human angiotensin-converting enzyme 2 transgenic mice. *Nat Commun* **11**:6122. doi:10.1038/s41467-020-19891-7

Oudit GY, Wang K, Viveiros A, Kellner MJ, Penninger JM. 2023. Angiotensin Converting Enzyme 2 - at the Heart of the COVID-19 pandemic. *Cell*. doi:10.1016/j.cell.2023.01.039

Pocha K, Mock A, Rapp C, Dettling S, Warta R, Geisenberger C, Jungk C, Martins LR, Grabe N, Reuss D, Debus J, Deimling A von, Abdollahi A, Unterberg A, Herold-Mende CC. 2020. Surfactant Expression Defines an Inflamed Subtype of Lung Adenocarcinoma Brain Metastases that Correlates with Prolonged Survival. *Clin Cancer Res* **26**:2231–2243. doi:10.1158/1078-0432.ccr-19-2184

Scheffzük C, Biedziak D, Gisch N, Goldmann T, Stamme C. 2024. Surfactant protein A modulates neuroinflammation in adult mice upon pulmonary infection. *Brain Res* **1840**:149108. doi:10.1016/j.brainres.2024.149108

Singh G, Diego JG-B, Warang P, Park S-C, Chang LA, Noureddine M, Laghlali G, Bykov Y, Prellberg M, Yan V, Singh S, Pache L, Cuadrado-Castano S, Webb B, García-Sastre A, Schotsaert M. 2024. Outcome of SARS-CoV-2 reinfection depends on genetic background in female mice. *Nat Commun* **15**:10178. doi:10.1038/s41467-024-54334-7

Snouwaert JN, Jania LA, Nguyen T, Martinez DR, Schäfer A, Catanzaro NJ, Gully KL, Baric RS, Heise M, Ferris MT, Anderson E, Pressey K, Dillard JA, Taft-Benz S, Baxter VK, Ting JP-Y, Koller BH. 2023. Human ACE2 expression, a major tropism determinant for SARS-CoV-2, is regulated by upstream and intragenic elements. *PLOS Pathog* **19**:e1011168. doi:10.1371/journal.ppat.1011168

Song I-W, Washington M, Leynes C, Hsu J, Rayavara K, Bae Y, Haelterman N, Chen Y, Jiang M-M, Drelich A, Tat V, Lanza DG, Lorenzo I, Heaney JD, Tseng C-TK, Lee B, Marom R. 2024. Generation of a humanized mAce2 and a conditional hACE2 mouse models permissive to SARS-COV-2 infection. *Mamm Genome* 1–9. doi:10.1007/s00335-024-10033-8

Stolp B, Stern M, Ambiel I, Hofmann K, Morath K, Gallucci L, Cortese M, Bartenschlager R, Ruggieri A, Graw F, Rudelius M, Keppler OT, Fackler OT. 2022. SARS-CoV-2 variants of concern display enhanced intrinsic pathogenic properties and expanded organ tropism in mouse models. *Cell Rep* **38**:110387. doi:10.1016/j.celrep.2022.110387

Sun J, Zhuang Z, Zheng J, Li K, Wong RL-Y, Liu D, Huang J, He J, Zhu A, Zhao Jingxian, Li X, Xi Y, Chen R, Alshukairi AN, Chen Z, Zhang Z, Chen C, Huang X, Li F, Lai X, Chen D, Wen L, Zhuo J, Zhang Y, Wang Y, Huang S, Dai J, Shi Y, Zheng K, Leidinger MR, Chen J, Li Y, Zhong N, Meyerholz DK, McCray PB, Perlman S, Zhao Jincun. 2020. Generation of a Broadly Useful Model for COVID-19 Pathogenesis, Vaccination, and Treatment. *Cell* **182**:734-743.e5. doi:10.1016/j.cell.2020.06.010

Varga Z, Flammer AJ, Steiger P, Haberecker M, Andermatt R, Zinkernagel AS, Mehra MR, Schuepbach RA, Ruschitzka F, Moch H. 2020. Endothelial cell infection and endotheliitis in COVID-19. *Lancet (Lond, Engl)* **395**:1417–1418. doi:10.1016/s0140-6736(20)30937-5

Winkler ES, Bailey AL, Kafai NM, Nair S, McCune BT, Yu J, Fox JM, Chen RE, Earnest JT, Keeler SP, Ritter JH, Kang L-I, Dort S, Robichaud A, Head R, Holtzman MJ, Diamond MS. 2020. SARS-CoV-2 infection of human ACE2-transgenic mice causes severe lung inflammation and impaired function. *Nat Immunol* **21**:1327–1335. doi:10.1038/s41590-020-0778-2

Wit E de, Doremalen N van, Falzarano D, Munster VJ. 2016. SARS and MERS: recent insights into emerging coronaviruses. *Nat Rev Microbiol* **14**:523–534. doi:10.1038/nrmicro.2016.81

Xu S, Ilyas I, Weng J. 2023. Endothelial dysfunction in COVID-19: an overview of evidence, biomarkers, mechanisms and potential therapies. *Acta Pharmacol Sin* **44**:695–709. doi:10.1038/s41401-022-00998-0

Zhang X, Liu J, Deng X, Bo L. 2024. Understanding COVID-19-associated endothelial dysfunction: role of PIEZO1 as a potential therapeutic target. *Front Immunol* **15**:1281263. doi:10.3389/fimmu.2024.1281263

A

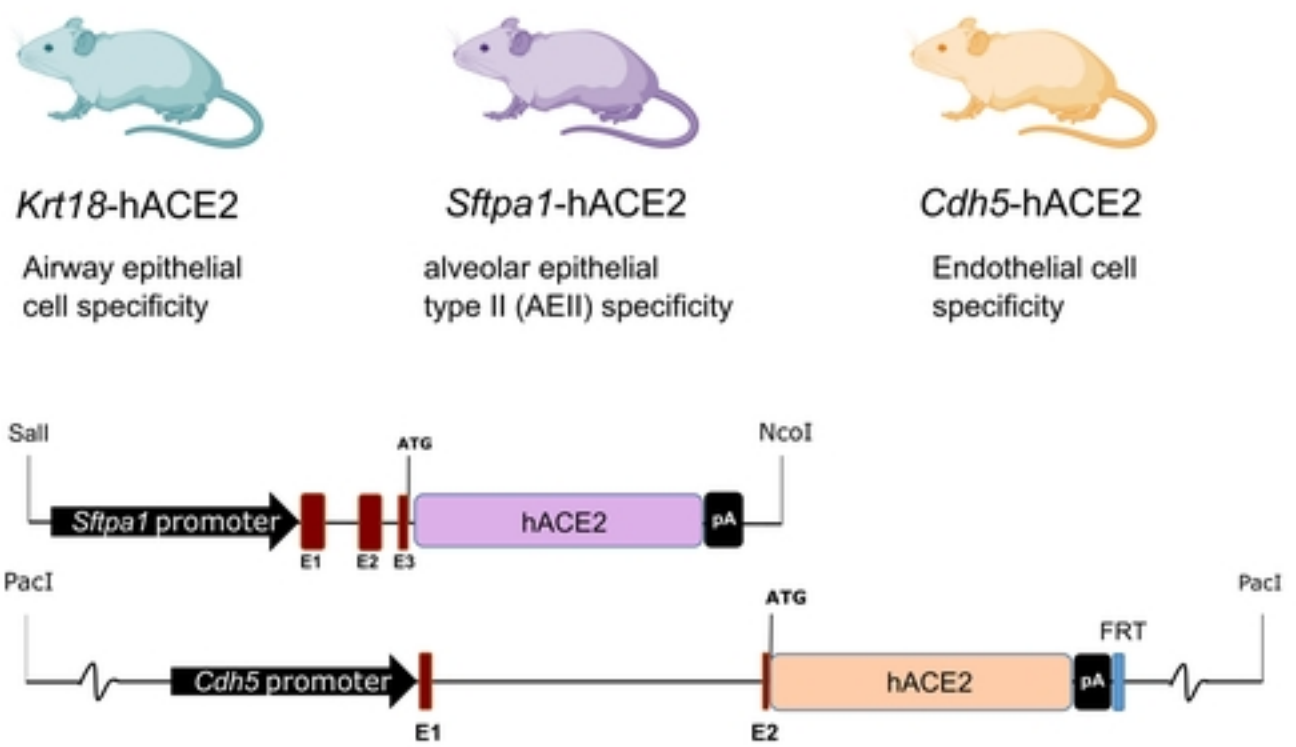
Krt18-hACE2
Airway epithelial cell specificity
Sftpa1-hACE2
alveolar epithelial type II (AEII) specificity
Cdh5-hACE2
Endothelial cell specificity
SalI
ATG
NcoI
Sftpa1 promoter
E1
E2
E3
hACE2
pA
PacI
ATG
PacI
FRT
Cdh5 promoter
hACE2
pA
E1
E2

B

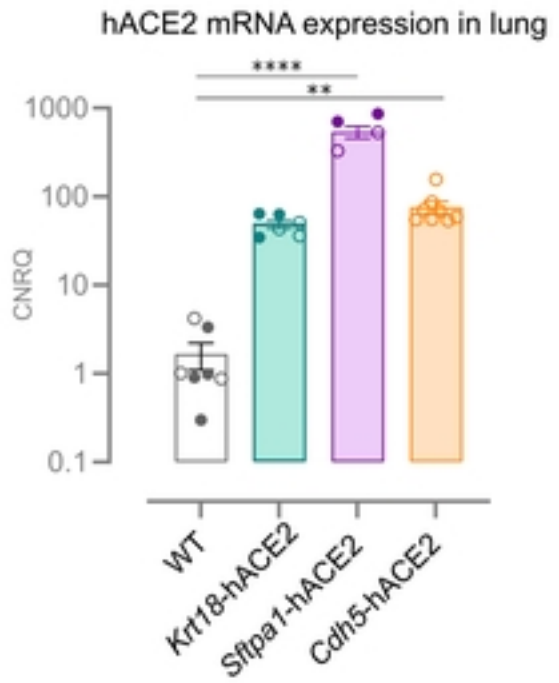
hACE2 mRNA expression in lung
****
**
1000
100
10
1
0.1
CNRQ
WT
Krt18-hACE2
Sftpa1-hACE2
Cdh5-hACE2

C

Krt18
Sftpa1
Cdh5
WT F M WT F M WT F M
LUNG
150
100
50
hACE2
Tubulin

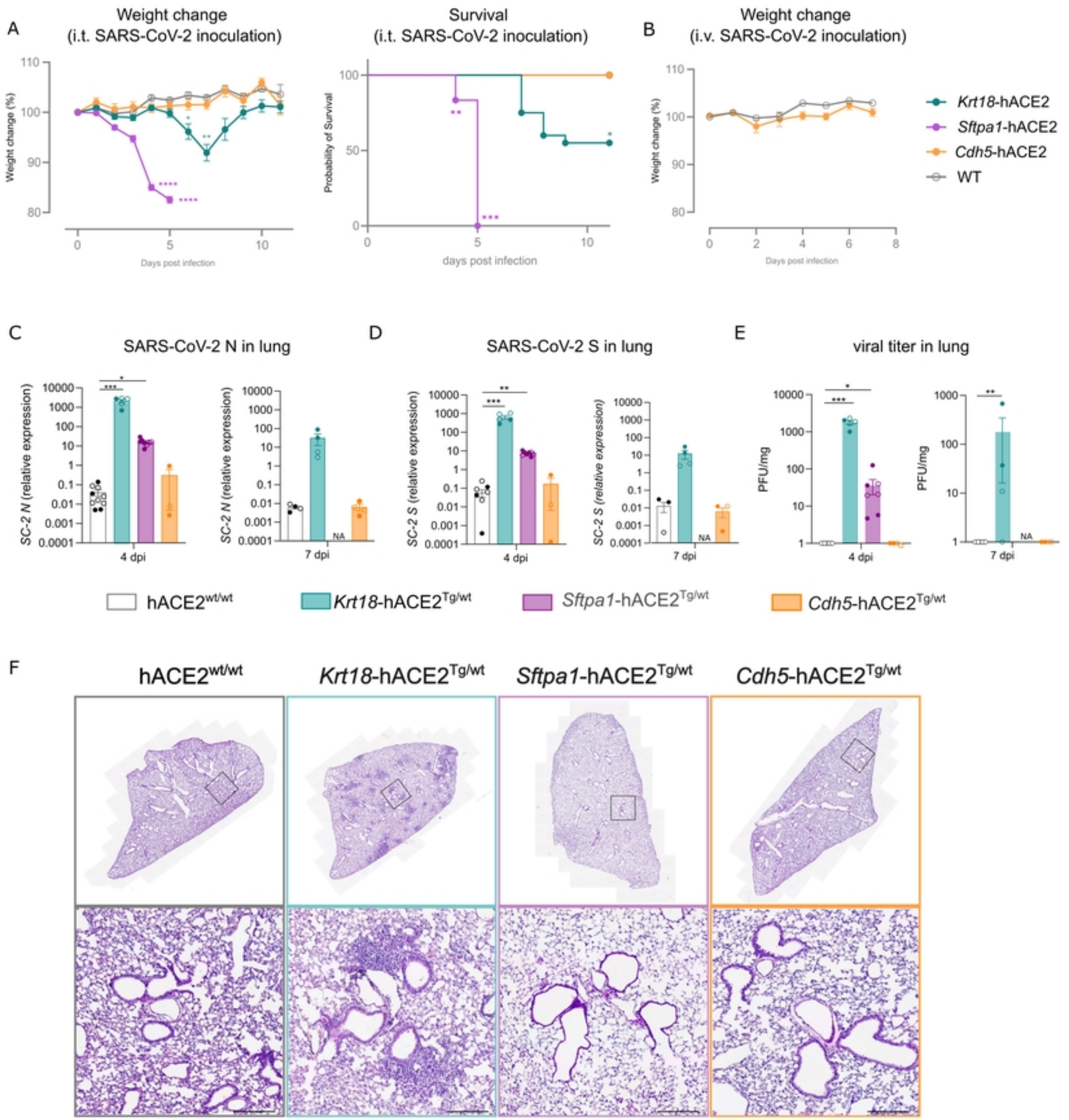
A
Weight change
(i.t. SARS-CoV-2 inoculation)
Weight change (%)
Days post infection
Survival
(i.t. SARS-CoV-2 inoculation)
Probability of Survival
days post infection
B
Weight change
(i.v. SARS-CoV-2 inoculation)
Weight change (%)
Days post infection
Krt18-hACE2
Sftpa1-hACE2
Cdh5-hACE2
WT
C
SARS-CoV-2 N in lung
SC-2 N (relative expression)
4 dpi
7 dpi
NA
D
SARS-CoV-2 S in lung
SC-2 S (relative expression)
4 dpi
7 dpi
NA
E
viral titer in lung
PFU/mg
4 dpi
7 dpi
NA
hACE2wt/wt
Krt18-hACE2Tg/wt
Sftpa1-hACE2Tg/wt
Cdh5-hACE2Tg/wt
F
hACE2wt/wt
Krt18-hACE2Tg/wt
Sftpa1-hACE2Tg/wt
Cdh5-hACE2Tg/wt

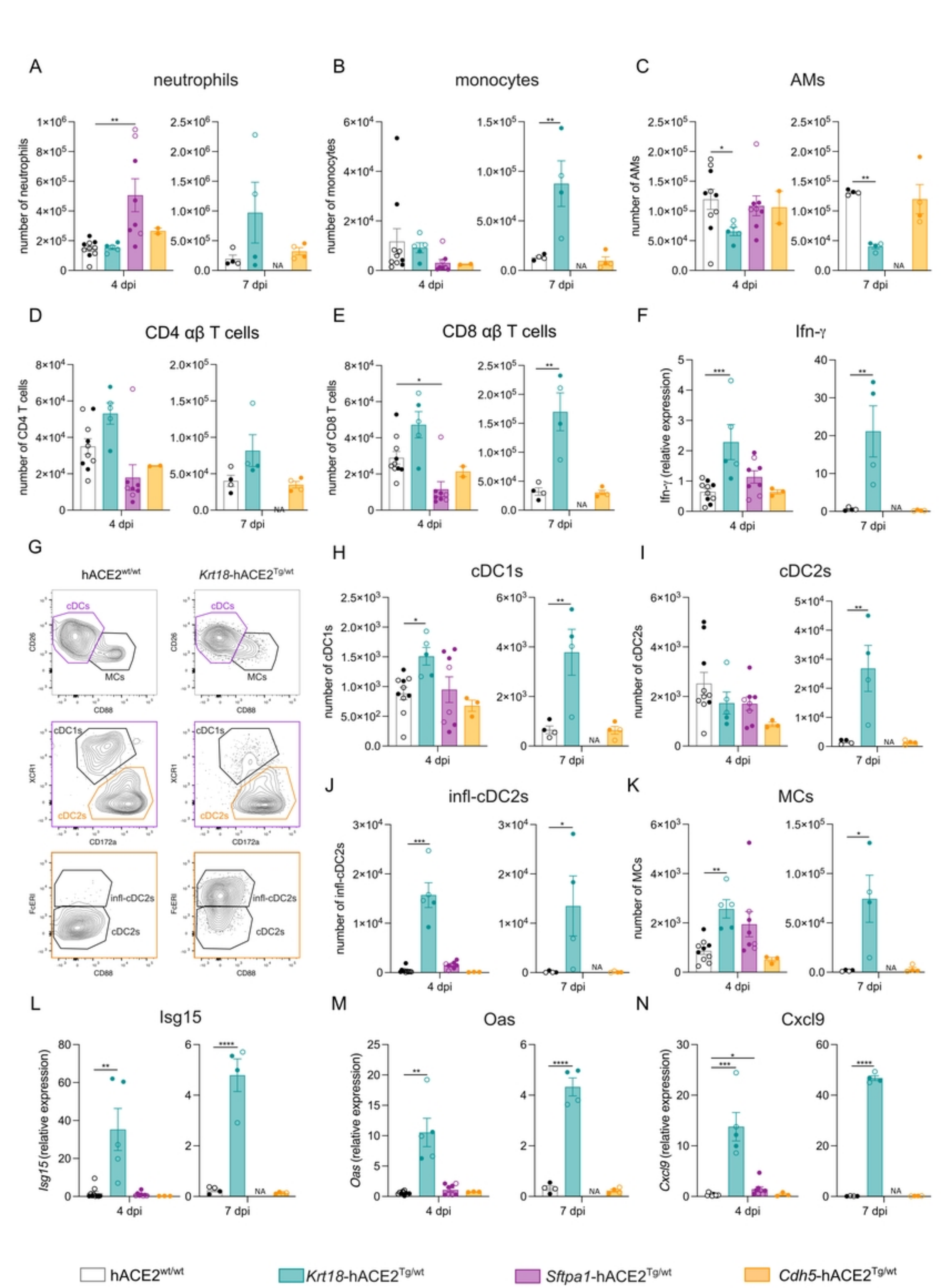
A
neutrophils
number of neutrophils
4 dpi
7 dpi
B
monocytes
number of monocytes
C
AMs
number of AMs
D
CD4 αβ T cells
number of CD4 T cells
E
CD8 αβ T cells
number of CD8 T cells
F
Ifn-γ
Ifn-γ (relative expression)
G
hACE2wt/wt
Krt18-hACE2Tg/wt
cDCs
MCs
cDC1s
cDC2s
infl-cDC2s
CD26
CD88
XCR1
CD172a
FcεRI
H
cDC1s
number of cDC1s
I
cDC2s
number of cDC2s
J
infl-cDC2s
number of infl-cDC2s
K
MCs
number of MCs
L
Isg15
Isg15 (relative expression)
M
Oas
Oas (relative expression)
N
Cxcl9
Cxcl9 (relative expression)
NA
hACE2wt/wt
Krt18-hACE2Tg/wt
Sftpa1-hACE2Tg/wt
Cdh5-hACE2Tg/wt

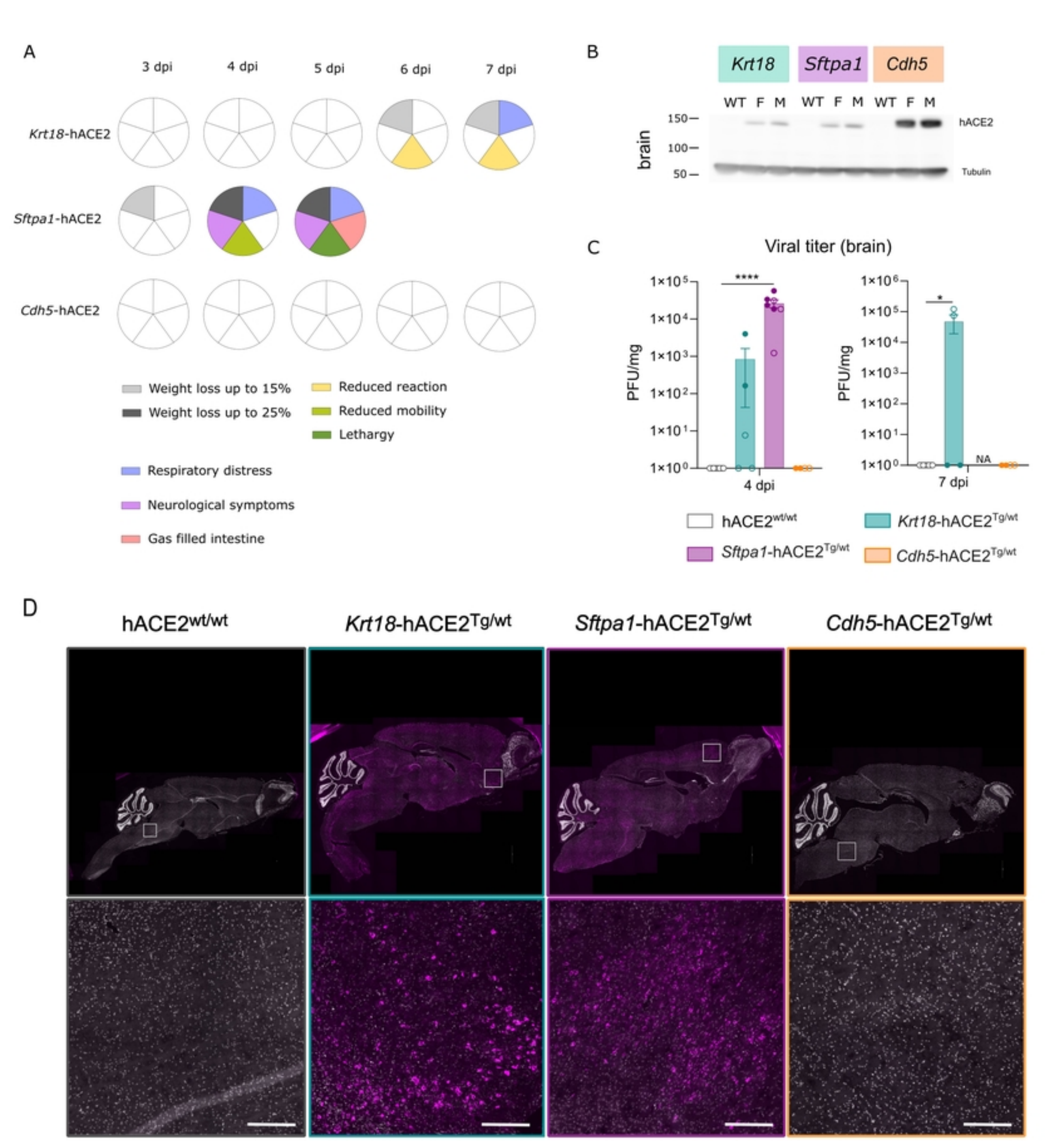
A
3 dpi
4 dpi
5 dpi
6 dpi
7 dpi
Krt18-hACE2
Sftpa1-hACE2
Cdh5-hACE2
Weight loss up to 15%
Weight loss up to 25%
Reduced reaction
Reduced mobility
Lethargy
Respiratory distress
Neurological symptoms
Gas filled intestine
B
Krt18
Sftpa1
Cdh5
WT F M WT F M WT F M
brain
150
100
50
hACE2
Tubulin
C
Viral titer (brain)
PFU/mg
4 dpi
7 dpi
NA
hACE2wt/wt
Krt18-hACE2Tg/wt
Sftpa1-hACE2Tg/wt
Cdh5-hACE2Tg/wt
D
hACE2wt/wt
Krt18-hACE2Tg/wt
Sftpa1-hACE2Tg/wt
Cdh5-hACE2Tg/wt

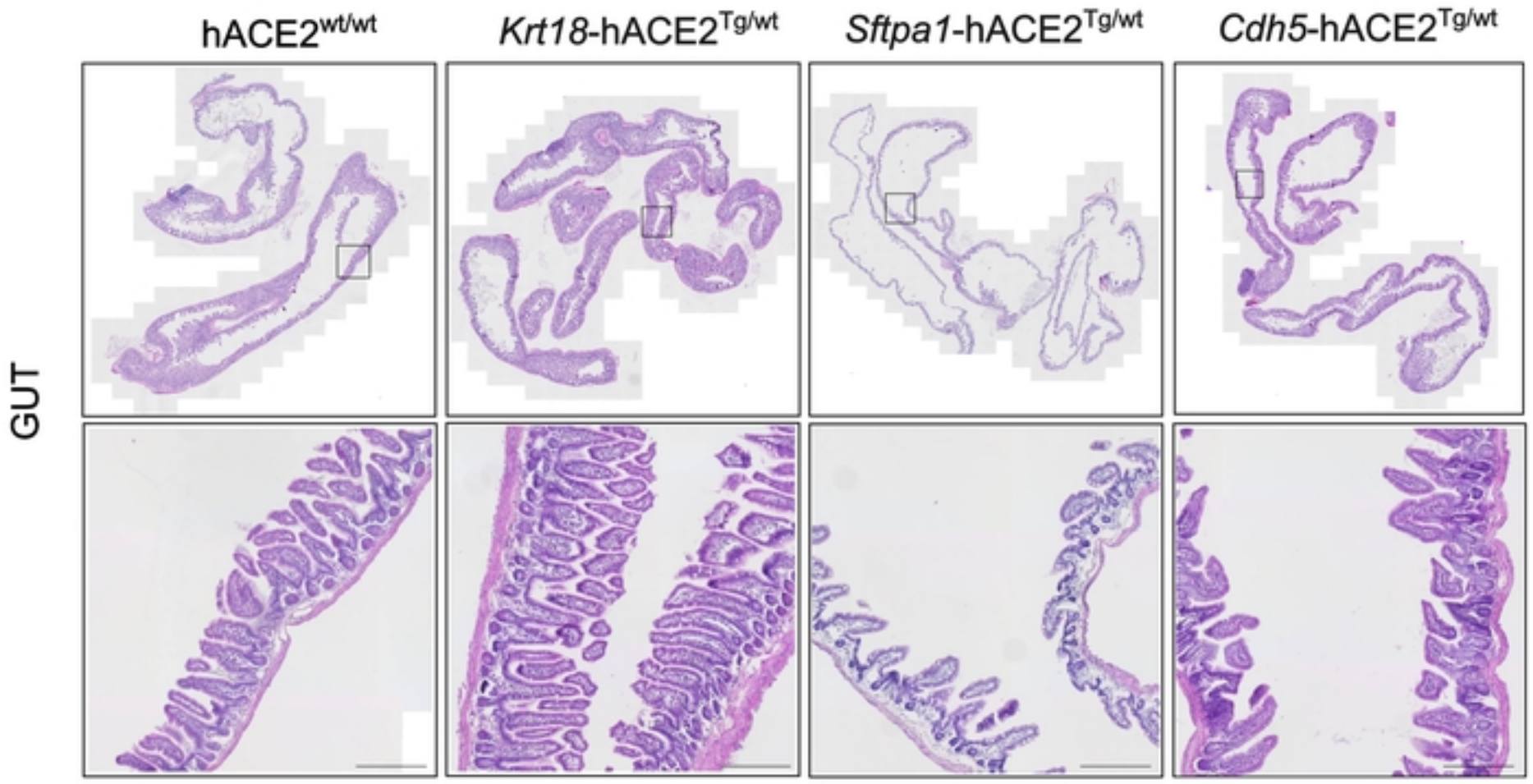
hACE2wt/wt
Krt18-hACE2Tg/wt
Sftpa1-hACE2Tg/wt
Cdh5-hACE2Tg/wt
GUT